



Analysis of Burr and Tear in Milling of Carbon Fiber Reinforced Plastic (CFRP) Using Finite Element Method

Fuji Wang¹ · Tianyu Gu¹ · Xiaonan Wang¹ · Xinghai Jin¹ · Boyu Zhang¹

Received: 16 November 2020 / Accepted: 22 March 2021 / Published online: 27 April 2021
© The Author(s), under exclusive licence to Springer Nature B.V. 2021

Abstract

Carbon fiber reinforced plastics (CFRPs) are vulnerable to the intralaminar damage (including burr and tear) and interlaminar damage (including delamination) during milling process. These damages will decrease the load carrying capability of the components. However, due to the different formation conditions and occurrence locations of the two types of damages, it is a challenge to accurately simulate them in a single model, which hinders the comprehensive understanding on the formation laws of CFRP milling damages. The present study establishes a novel three-dimensional macroscopic milling model, which predicts both the interlaminar fracture and intralaminar cracking of the CFRP. The cohesive elements are applied to model the interlaminar fracture. The intralaminar cracking is also simulated by inserting cohesive elements in the top layer of CFRP along the fiber direction, and the insert interval is adjusted for an enhanced accuracy of the model. Furthermore, a Python script is defined to improve the efficiency of establishing the model. Through the calculation of the models, the cutting forces and the damage extents at four typical fiber orientation angles (FOAs) are both accurately calculated. Moreover, the formation laws of CFRP milling damages are specifically analyzed. Results suggest that the burr and tear damages become serious with the increase of the FOA. The developed model is helpful for further understanding the formation mechanisms of the intralaminar damage, and it is expected that the findings can provide relevant technical supports for the suppression of CFRP milling damage.

Keyword CFRP · Simulation · Burr · Tear · Cohesive element · Script

1 Introduction

Carbon fiber reinforced plastics (CFRPs) have been widely used in aerospace and military applications due to their excellent mechanical properties such as high specific strength and specific modulus, enhanced wear resistance, and etc. [1–4]. In the manufacturing of the

✉ Fuji Wang
wfjsll@dlut.edu.cn

¹ Key Laboratory for Precision and Non-Traditional Machining Technology of the Ministry of Education, School of Mechanical Engineering, Dalian University of Technology, Dalian 116024, China

CFRPs, a lot of milling processes are needed to assure that the components meet the desired dimensional tolerance and surface quality [5, 6]. However, due to the anisotropy and heterogeneity characteristics of CFRPs, the burr, tear and delamination are generated easily during milling [7], resulting in a decrease in the bearing capacity and reliability of CFRP parts. Delamination would reduce the stiffness and the load-carrying capacity of the mechanical parts [8]. Due to pulling out of the fiber, tear destroys the structural integrity of CFRP components, thus tear reduces the bearing capacity and the lifespan of the components [9]. Furthermore, the burrs are the most frequent surface damage during milling of CFRP laminates, and their appearance may cause several problems. For example, increasing the cost and the time of production due to additional machining and degrading the safety of composite components owing to burrs growth resulting from the unpredictable deburring process [10]. Therefore, it is necessary to study the damage formation mechanism in the CFRP milling and suppress these damages to fully apply the excellent mechanical properties of CFRPs.

The damage in the CFRP milling was usually studied through the experimental method. Ramulu et al. [11] conducted a lot of milling experiments, and it was found that the damage mainly appeared at the external layers of the workpiece. Hintze et al. [12] analyzed the influences of tool wear and fiber cutting angle on the surface damage in the CFRP milling. Haddad et al. [13] studied the effect of milling damage on the bearing capacity, and the results showed the damage reduced the bearing capacity. The above researches discovered that the burr and tear mainly occurred at the external layers of the CFRPs (also known as the surface damage), and they analyzed the influences of the processing parameters and cutter geometry on the damage. However, the formation process of the surface damage has not been researched in detail, therefore, it is necessary to further reveal the formation mechanism of the surface damage in the CFRP milling and help to provide relevant theoretical guidance for the improvement of the machining quality.

Studying the surface damages only through experiments requires tremendous amount of trials for different processing parameters. It is time-consuming and the research cost would be quite expensive. Moreover, because the cutting speed is extremely fast in CFRP milling, it is intractable to monitor the cutting process and damage propagation during the experiment. The finite element (FE) analysis is suitable for the investigation of the formation mechanism of surface damage, which can effectively simulate the cutting process and then observe the damage propagation. At present, the numerical simulation model for the composites cutting can be classified into macro and micro models. These models have been widely used to research the damage of composite materials. Wang et al. [14] established two-dimensional (2D) macroscopic and microscopic models to analyze the removal mechanism of CFRPs and the chip formation process. Hassouna et al. [15] developed a 2D macro-model to study the effects of mechanical properties and hourglass control on the cutting process of CFRPs. Three-dimensional (3D) FE models were allowed to develop owing to the improvement of computer power. Liu et al. [16] used a 3D micro-model to reveal the underlying cutting damage mechanism of composites during the machining process. Zhang et al. [17] proposed a 3D macro-model to explore the impact mechanism of fiber cutting angle and cutting parameters on cutting force, stress, material failure, and the material removal mechanism in high-speed cutting of CFRP were revealed. 3D FE models for the investigation of the CFRP drilling were reported by Phadnis [18] and Isbilir [19] et al., with these models, the variations of thrust force, torque and delamination with the step ratio of step drill and the processing parameters were analyzed. Feito et al. [20] established 3D models to assess the thrust force and delamination when the CFRPs were processed by twist drill and step drill at different feed rates and cutting speeds. He et al. [21] proposed a 3D numerical model for the prediction of the unidirectional CFRP milling. In

this work, the delamination was simulated based on the cohesive elements. Prakash et al. [22] analyzed the impacts of feed rate and spindle speed on the milling force and chip formation by a 3D model. In summary, most numerical simulation models focus on orthogonal cutting or drilling operations. However, there are few simulations related to the CFRP milling. Moreover, the current studies related to the CFRP milling simulation are mainly focused on the delamination. There are still no 3D FE models to precisely simulate the formation process of surface damage in the CFRP milling, so it is imperative to develop a new 3D milling model to reveal the damage mechanism of surface damage.

In this study, a 3D FE model for the CFRP milling is developed to reveal the formation mechanism of the surface damage. Since burr and tear are mainly affected by the intralaminar cracking that appeared and propagated along the fiber direction within the surface layers, the cohesive elements are inserted in the surface along the fiber direction to simulate the intralaminar cracking and assumed to have equally spaced internal. Meanwhile, the material behavior of the layer interface is also characterized by the cohesive elements so as to model the delamination. Aiming to improve the efficiency of establishing the model, a Python script is defined for the model development. The model is verified through experiments, and it helps to assess the cutting forces, burr and tear damages at four typical fiber orientation angles (FOAs).

The rest of this paper is laid out as follows. The details of the FE model for the CFRP milling are presented in the second section. Experimental work required for the model validation is given in Sect. 3. The simulation and experimental results are compared and discussed in the fourth section. Finally, conclusions are provided at the end of this paper.

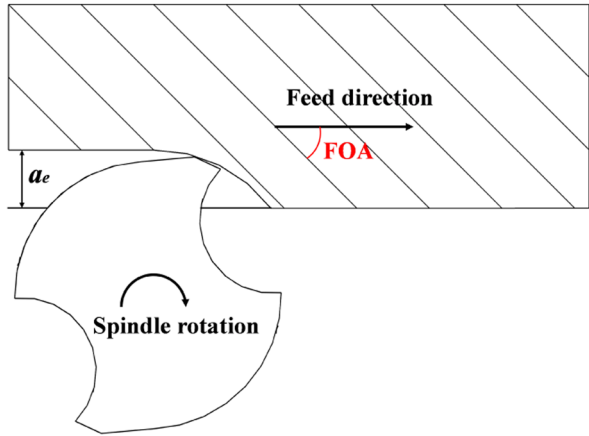
2 Finite Element Model

This section describes the Python script used for the development of the FE model in detail. The material models, boundary conditions and tool-workpiece interactions applied in this work to predict the milling of unidirectional CFRPs are also introduced.

2.1 Python Script for the FE Modeling

The surface damage of the unidirectional (UD) CFRPs is affected by the FOA and the four FOAs of 0° , 45° , 90° , 135° are the common layup configuration. In the paper, FOA is defined from the front view of the workpiece, and measured clockwise with reference to the feed direction, as shown in Fig. 1. In order to simulate the surface damage under the four typical FOAs, four models with different geometry structures are presented. As the Abaqus/Explicit module has advantages in solving the nonlinear dynamic process of CFRPs cutting, the models are built by the commercial software Abaqus. The development of the milling model with cohesive elements in the surface includes the establishment of the workpiece geometric model, the meshing of the elements and the setting of the material models. To strike a balance between the calculation cost and simulation accuracy, the geometric model of the workpiece is simplified to have four layers with the same thickness (T). Meanwhile, the cohesive elements are inserted in the top layer of the CFRPs and presumed to have equal intervals to model intralaminar cracking. According to the Abaqus/Explicit module, it would be better to create the cohesive element by offsetting the external surface of a meshed element. Therefore, in the establishment of the top layer, a large number (N) of

Fig. 1 FOA definition



blocks are built and meshed to facilitate the generation of the cohesive element, as shown in Fig. 2. The external surface of these blocks that utilized to develop the cohesive element is parallel to the fiber direction, thus the simulated interface would crack along the fiber direction. Additionally, the width (W) of these blocks is determined by the insert interval of the cohesive elements. In this case, the number of elements in each block along the transverse

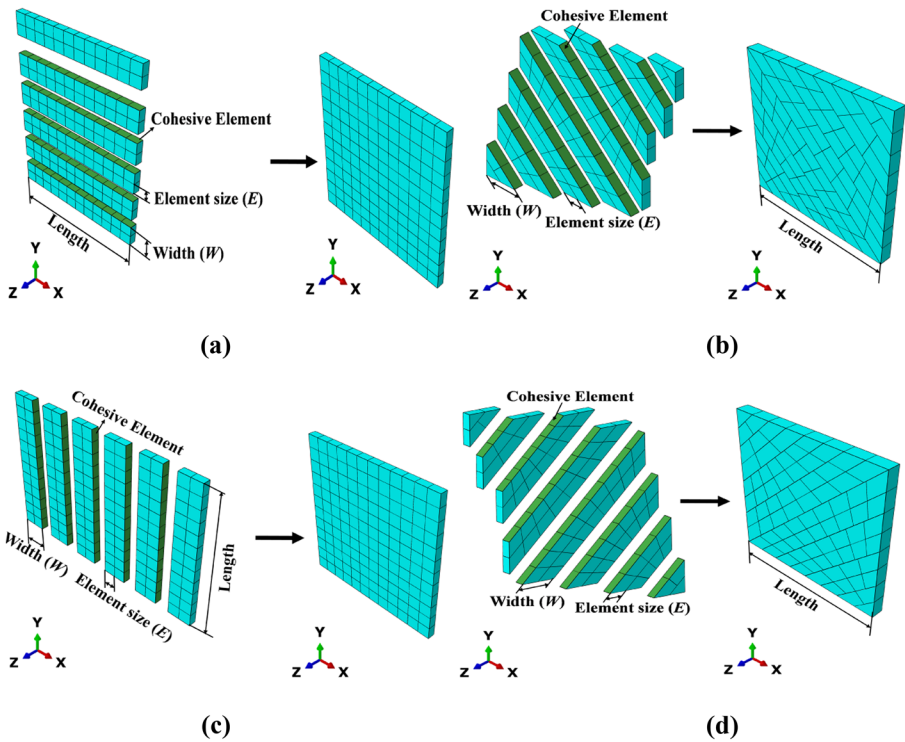


Fig. 2 Top layer geometry model with four typical FOAs: (a) 0° FOA CFRPs; (b) 45° FOA CFRPs; (c) 90° FOA CFRPs; (d) 135° FOA CFRPs

direction could be determined by W and the element size (E), as given in Eq. (1). The other three layers of the workpiece are not considered to simulate the intralaminar cracking, therefore, they are created as solid parts with no cohesive elements inserted. Moreover, the element type of the meshes in the blocks and the other three layers is 8-node linear brick element with reduced integration (C3D8R), while zero-thickness 8-node 3D cohesive elements (COH3D8) are used to model the layer interfaces and the interfaces within the top layer.

$$s = \frac{W}{E} \tag{1}$$

where S is the number of elements in each block along the transverse direction.

The geometric model with cohesive elements in the top layer is complex, and the different blocks in the top layer with different FOAs make the geometry model more complex. Thus, it takes a long time to build the FE model. Furthermore, it is necessary to adjust the insert interval of cohesive elements in the top layer to improve the simulation accuracy, which also requires a lot of time. Therefore, in order to realize parametric modeling of the CFRP milling thus increase the modeling efficiency, a Python script for developing the model is defined. The establishment process of the FE model is shown in Fig. 3.

The Python script separately creates the geometric models of the blocks in the top layer and the other three layers. Building the geometry models of the blocks requires obtaining their coordinates. As the coordinates of all blocks in the z -direction maintain invariable, the key to establishing the geometric models is how to obtain the coordinates of the blocks in

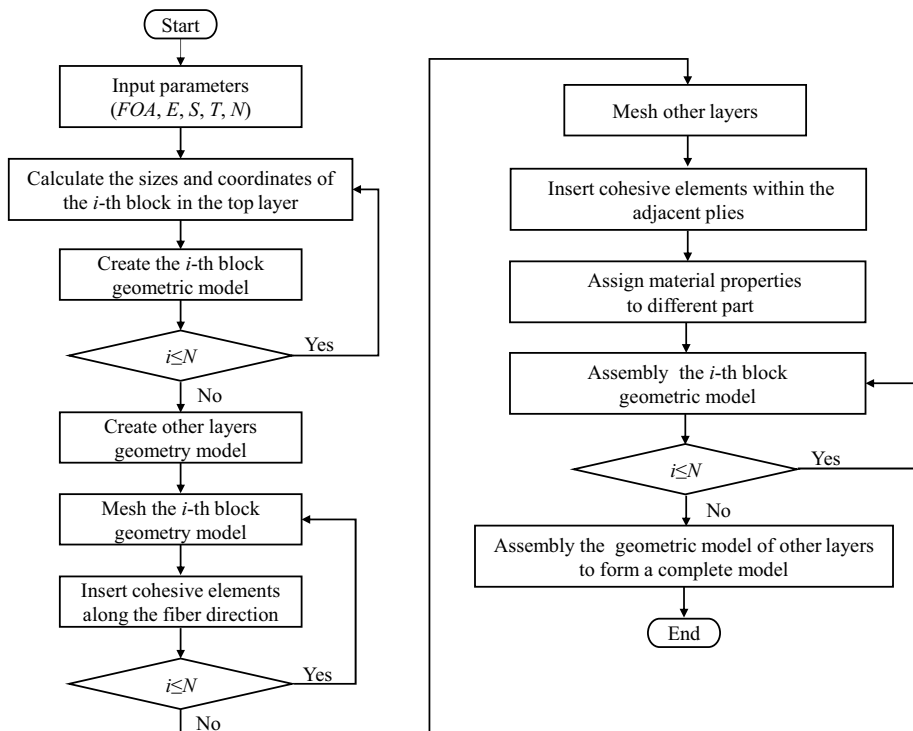


Fig. 3 Flow chart for establishing FE model

the x - y plane. Firstly, a coordinate system O - xyz is defined, wherein the x - y plane is set as the sketch plane and the z -direction is treated as the through-thickness direction. Secondly, the geometric models of the CFRPs workpieces with the four typical FOAs are built based on the above-mentioned parameters. The sketches of the blocks in the top layer of the 0° and 90° FOAs CFRPs are all rectangles, and the length and width of them are $E \times S \times N$ and $E \times S$. For the 0° FOA CFRPs, the coordinates of the four points of the first block are set as $A1(0, 0)$, $B1(E \times S \times N, 0)$, $C1(0, E \times S)$, $D1(E \times S \times N, E \times S)$. Then, the coordinates of the four points of the second block ($A2, B2, C2$, and $D2$) are obtained by adding $E \times S$ on the y coordinates of $A1, B1, C1$, and $D1$, respectively, where $A2, B2$ coincide with $C1, D1$. Similarly, the y coordinates of the four points of the $(i-1)$ -th block increase $E \times S$ to gain the coordinates of Ai, Bi, Ci , and Di , as shown in Fig. 4a. Using the same calculation method, the coordinates of the four points of all the blocks in the top layer of 90° FOA CFRPs are deduced, as shown in Fig. 4c. The coordinates of i -th ($i = 1, 2 \dots n \dots N$) block in the top layer of 0° and 90° FOA CFRPs are given in Eq. (2).

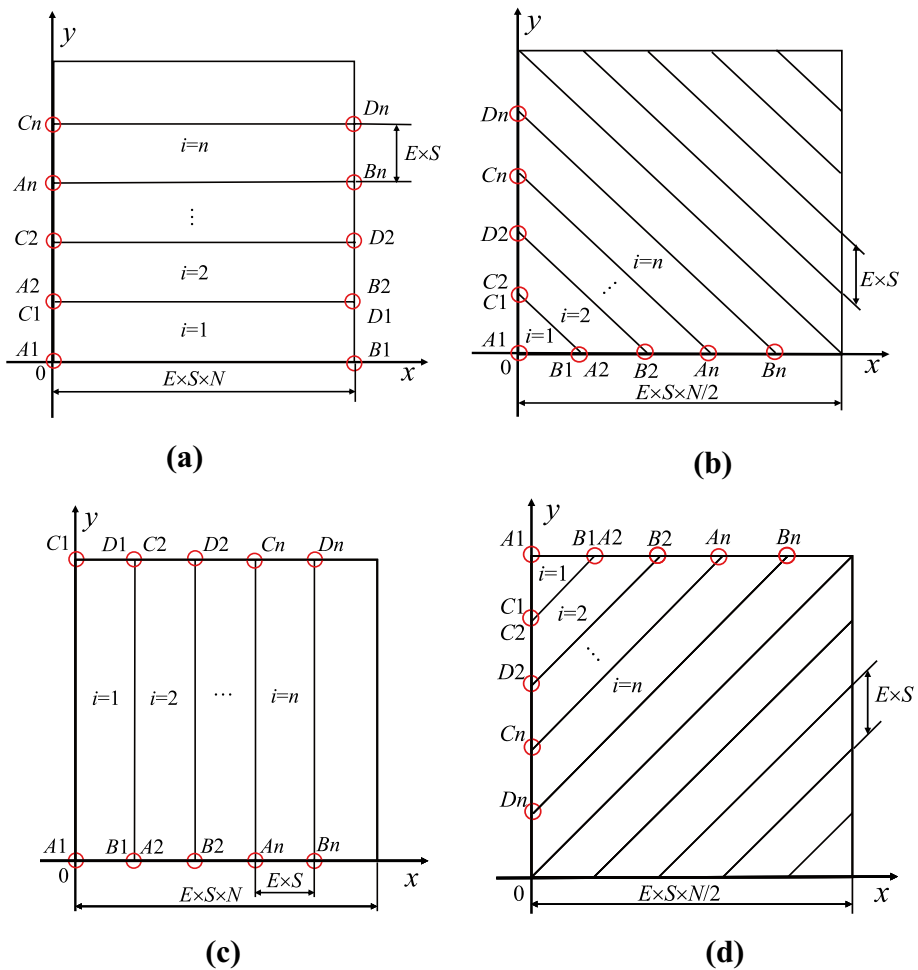


Fig. 4 Schematic diagram of the top layer of the four typical FOAs CFRPs: (a) 0° FOA CFRPs; (b) 45° FOA CFRPs; (c) 90° FOA CFRPs; (d) 135° FOA CFRPs

$$\begin{aligned}
 &0^\circ \text{ FOA CFRPs} \\
 &\left\{ \begin{array}{l} (0, 0) \\ (E \times S \times N, 0) \\ (0, E \times S) \\ (E \times S \times N, E \times S) \end{array} \right. \quad (i = 1) \left\{ \begin{array}{l} (0, E \times S) \\ (E \times S \times N, E \times S) \\ (0, E \times S \times 2) \\ (E \times S \times N, E \times S \times 2) \end{array} \right. \quad (i = 2) \dots \left\{ \begin{array}{l} (0, E \times S \times (i = 1)) \\ (E \times S \times N, E \times S \times (i = 1)) \\ (0, E \times S \times i) \\ (E \times S \times N, E \times S \times i) \end{array} \right. \quad (i = 3, 4 \dots N) \\
 &90^\circ \text{ FOA CFRPs} \\
 &\left\{ \begin{array}{l} (0, 0) \\ (E \times S, 0) \\ (0, E \times S \times N) \\ (E \times S, E \times S \times N) \end{array} \right. \quad (i = 1) \left\{ \begin{array}{l} (E \times S, 0) \\ (E \times S \times 2, 0) \\ (E \times S, E \times S \times N) \\ (E \times S \times 2, E \times S \times N) \end{array} \right. \quad (i = 2) \dots \left\{ \begin{array}{l} (E \times S \times (i = 1), 0) \\ (E \times S \times i, 0) \\ (E \times S \times (i = 1), E \times S \times N) \\ (E \times S \times i, E \times S \times N) \end{array} \right. \quad (i = 3, 4 \dots N)
 \end{aligned} \tag{2}$$

Since the geometric models of the top layer of 45° and 135° FOAs CFRPs are composed of blocks along the fiber direction, the sketches of the first and last blocks are right triangles, while the sketches of the rest blocks are trapezoidal. Regarding the 45° FOA CFRPs, the coordinates of the three points of the first block are set as A1 (0, 0), B1 (E×S, 0), C1 (0, E×S). The x coordinates of the A1 and B1 are increased by E×S in the x-axis direction to obtain the coordinates of A2 and B2. Meanwhile, the y coordinates of the A1 and C1 are added by E×S in the y-axis direction to gain the coordinates of C2 and D2, where B1, C1 coincide with A2, C2. Similarly, the x coordinates of the two points of the (i-1)-th block are increased by E×S in the x-axis direction to acquire the coordinates of Ai and Bi. The y coordinates of the two points of the (i-1)-th block are added by E×S in the y-axis direction to deduce the coordinates of Ci and Di, as shown in Fig. 4b. The geometric models of the top layer of 135° FOA CFRPs are similar to that of the 45° FOA CFRPs, as shown in Fig. 4d. The coordinates of i-th (i=1, 2···N) block in the top layer of 45° and 135° FOA CFRPs

45° FOA CFRPs

$$\begin{aligned}
 &\left\{ \begin{array}{l} (0,0) \\ (E \times S, 0) \\ (0, E \times S) \end{array} \right. \quad (i = 1) \dots \left\{ \begin{array}{l} ((i = 1) \times E \times S, 0) \\ (i \times E \times S, 0) \\ (0, (i = 1) \times E \times S) \\ (0, i \times E \times S) \end{array} \right. \quad (i = 2, 3 \dots N/2) \\
 &\left\{ \begin{array}{l} ((i - N/2) \times E \times S, E \times S \times N/2) \\ ((i - N/2) \times E \times S, E \times S \times N/2) \\ (E \times S \times N/2, (i - N/2 - 1) \times E \times S) \\ (E \times S \times N/2, (i - N/2) \times E \times S) \end{array} \right. \quad (i = N/2 \dots N - 1) \left\{ \begin{array}{l} (E \times S \times N/2, E \times S \times N/2) \\ (E \times S \times (N/2 - 1), E \times S \times N/2) \\ (E \times S \times N/2, E \times S \times ((N/2 - 1))) \end{array} \right. \quad (i = N)
 \end{aligned}$$

135° FOA CFRPs

$$\begin{aligned}
 &\left\{ \begin{array}{l} (0, E \times S \times N/2) \\ (E \times S, E \times S \times N/2) \\ (0, E \times S \times (N/2 - 1)) \end{array} \right. \quad (i = 1) \dots \left\{ \begin{array}{l} (E \times S \times (i - 1), E \times S \times N/2) \\ (E \times S \times i, E \times S \times N/2) \\ (0, E \times S \times (N/2 - i + 1)) \\ (0, E \times S \times (N/2 - i)) \end{array} \right. \quad (i = 2, 3 \dots N/2) \\
 &\left\{ \begin{array}{l} ((i - N/2 - 1) \times E \times S, 0) \\ ((i - N/2) \times E \times S, 0) \\ (E \times S \times N/2, (N - i - 1) \times E \times S) \\ (E \times S \times N/2, (N - i) \times E \times S) \end{array} \right. \quad (i = N/2 \dots N - 1) \left\{ \begin{array}{l} (E \times S \times N, 0) \\ (E \times S \times (N/2 - 1), 0) \\ (E \times S \times N/2, E \times S) \end{array} \right. \quad (i = N)
 \end{aligned} \tag{3}$$

are given in Eq. (3). After developing the geometric model of the top layer, the other three layers of UD-CFRPs could be built by just input the dimension of the whole layer.

All the blocks in the top layer are meshed with the same size to improve the accuracy of the surface damage simulation. Meanwhile, fine meshes are set in the cutting area of the other three layers while coarse elements are present in the non-cutting area to improve the computational efficiency. In addition, the Python script helps to assign corresponding material properties to the different parts. The material parameters would be introduced in the next section.

In order to facilitate the operation and parametric modeling, the graphical user interface (GUI) is designed to be associated with the Python script to build the model, as shown in Fig. 5. The input parameters of the GUI include FOA , E , S , T and N . After passing these parameters to the Python script, the FE model can be established, as shown in Fig. 6.

2.2 Material Models

The cutting of CFRPs is a complex and progressive damage process, it usually shows complicated damage modes, such as fiber fracture, matrix cracking, etc. [23–25]. In order to effectively simulate the material removal process in CFRP milling, the workpiece is modeled as an equivalent homogeneous material (EHM) which exhibits linear elastic orthotropic material behavior before damage. According to the relevant studies on the damage initiation criterion of the composite material, the Hashin criteria [26, 27] have been widely applied to predict the damage initiation of the CFRPs and separately model four distinct failure modes: fiber tension failure, fiber compression failure, matrix tensile failure, matrix compressive failure. However, the researchers found that the Hashin criteria cannot accurately predict the matrix compressive damage initiation [24, 31]. Thus, the criteria used for evaluating the damage initiation are based on Hashin and Puck failure criteria [28, 29]. In the paper, the Hashin criteria are used to estimate the fiber breakage and matrix tensile damage initiation [24, 27], while the damage model developed by Puck [30] is used to model matrix compressive failure [28, 29], as shown in Eqs. (4)–(7).

Fiber tensile failure($\sigma_{11} \geq 0$):

$$F_{ft} = \left(\frac{\sigma_{11}}{X^T} \right)^2 + \left(\frac{\tau_{12}}{S_{12}} \right)^2 + \left(\frac{\tau_{13}}{S_{13}} \right)^2 = 1 \quad (4)$$

Fiber compressive failure($\sigma_{11} < 0$):

$$F_{fc} = \left(\frac{\sigma_{11}}{X^C} \right)^2 = 1 \quad (5)$$

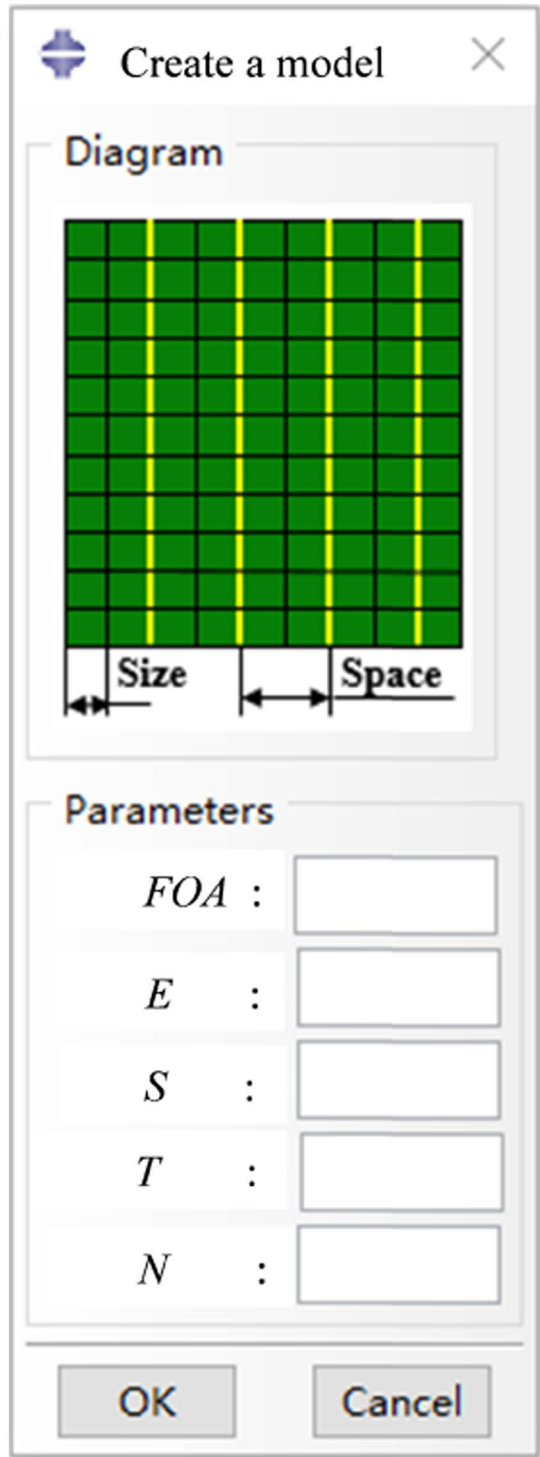
Matrix tensile failure($\sigma_{22} \geq 0$):

$$F_{mt} = \left(\frac{\sigma_{22}}{Y^T} \right)^2 + \left(\frac{\tau_{12}}{S_{12}} \right)^2 + \left(\frac{\tau_{23}}{S_{23}} \right)^2 = 1 \quad (6)$$

Matrix compressive failure($\sigma_{22} < 0$):

$$F_{mc} = \left(\frac{\tau_{nt}}{S_{23}^A + \mu_{nt}\sigma_{nn}} \right)^2 + \left(\frac{\tau_{nl}}{S_{12} + \mu_{nl}\sigma_{nn}} \right)^2 = 1 \quad (7)$$

Fig. 5 GUI interface for establishing geometric model of the workpiece



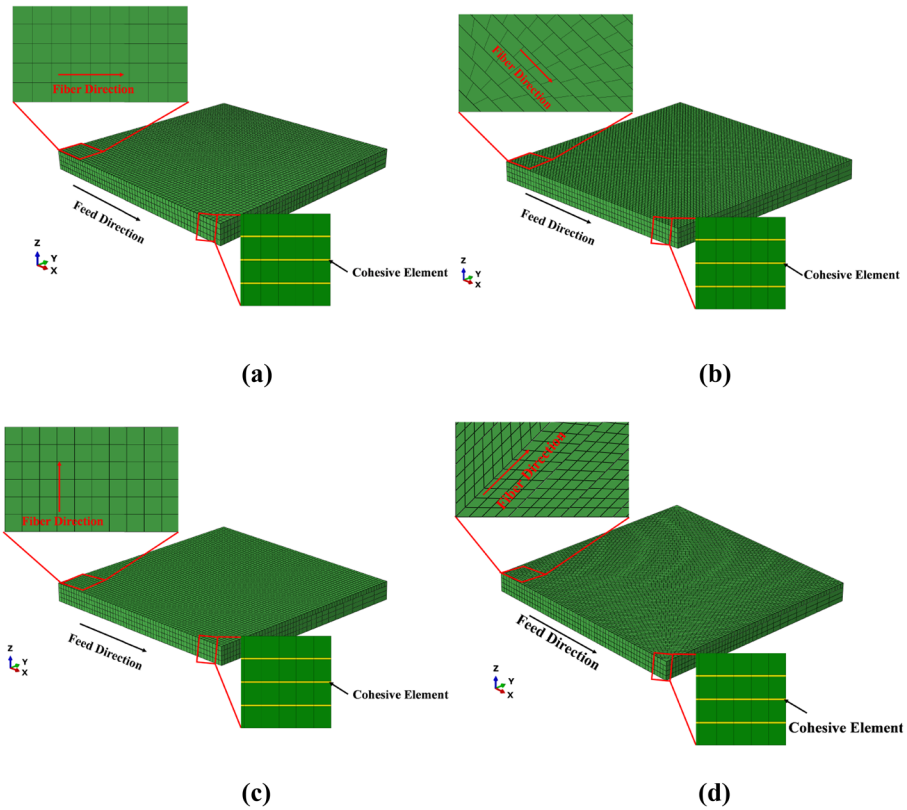


Fig. 6 CFRP models of four typical FOAs: (a) 0° FOA CFRPs; (b) 45° FOA CFRPs; (c) 90° FOA CFRPs; (d) 135° FOA CFRPs

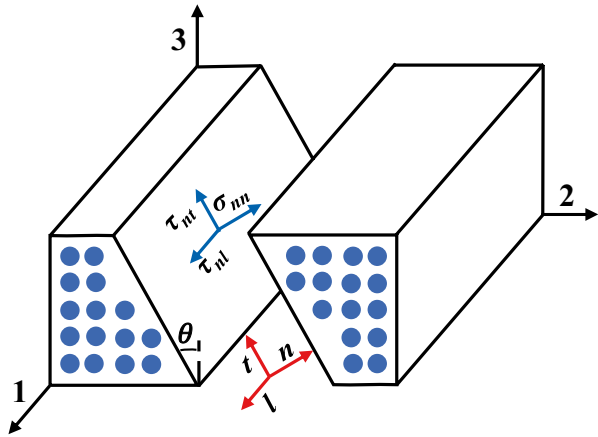
where, σ_{ii} and τ_{ij} ($i, j=1, 2, 3$) are the normal and shear effective stress tensor, X^T and X^C denote the tensile and compressive strengths of the unidirectional composite laminate in the fiber direction. Y^T and Y^C are the tensile and compressive strengths in the transverse direction. S_{ij} represents the longitudinal and transverse shear strengths of the composite. S_{23}^A is the transverse shear strength in the fracture plane, which can be determined by the transverse compression strength and the angle of fracture plane. It has been experimentally observed that matrix compressive damage occurs along a fracture plane oriented at $\theta=53^\circ$ [31] with respect to the through-thickness direction, as shown in Fig. 7. Where 1, 2, 3 represent the longitudinal, transverse and through-thickness directions respectively, S_{23}^A is expressed as:

$$S_{23}^A = \frac{Y_c}{2} \left(\frac{1 - \sin(\phi)}{\cos(\phi)} \right) \tag{8}$$

ϕ is determined by the fracture angle θ . $\phi = 2\theta - 90^\circ$

σ_{nn} , τ_{nl} and τ_{nt} are the stress components in the normal, longitudinal, and tangential directions of the fracture surface, which can be obtained as a function of the effective stress tensors [32].

Fig. 7 Fracture plane defined for matrix compressive damage



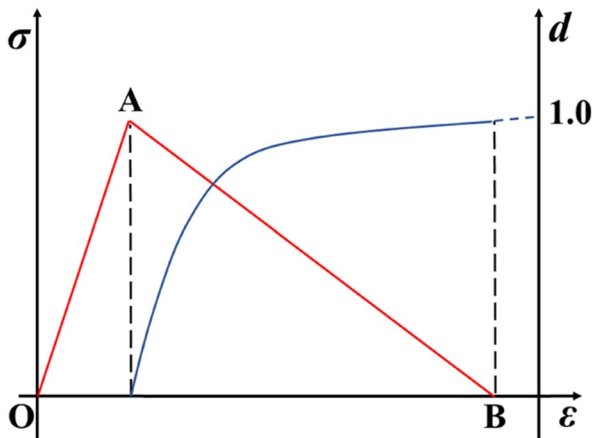
$$\begin{aligned}
 \sigma_{nn} &= \sigma_{22} \cos^2 \theta + \sigma_{33} \sin^2 \theta + 2\tau_{23} \sin \theta \cos \theta \\
 \tau_{nt} &= \tau_{31} \sin \theta + \tau_{21} \cos \theta \\
 \tau_{nl} &= (\sigma_{33} - \sigma_{22}) \sin \theta \cos \theta + \tau_{23} (\cos^2 \theta - \sin^2 \theta)
 \end{aligned}
 \tag{9}$$

μ_{nt} and μ_{nl} are the friction coefficients which can be defined based on the fracture angle and material property referring to the Mohr–Coulomb failure theory [24].

$$\mu_{nt} = \tan(\phi), \quad \frac{\mu_{nt}}{S_{23}^A} = \frac{\mu_{nl}}{S_{12}}
 \tag{10}$$

Once damage occurs, the element stiffness begins to degrade according to the linear damage evolution laws. When the damage initiation criteria Eqs. (4)–(7) are satisfied (point A in Fig. 8), the material properties are gradually degraded. The damage variable d in the corresponding damage mode starts to increase from zero, which is continuously

Fig. 8 Material behavior of the EHM



updated by the FE approach with increasing applied load. When d approaches one, the stiffness of the element degrades to zero and the material fails completely.

For fiber and matrix tensile failure, the damage variable d is expressed as [33]:

$$\begin{aligned}
 d_f^T &= \frac{\epsilon_f^{fT}}{\epsilon_f^{fT} - \epsilon_f^{0T}} \left(1 - \frac{\epsilon_f^{0T}}{\epsilon_f} \right) \\
 d_m^T &= \frac{\epsilon_m^{fT}}{\epsilon_m^{fT} - \epsilon_m^{0T}} \left(1 - \frac{\epsilon_m^{0T}}{\epsilon_m} \right)
 \end{aligned}
 \tag{11}$$

Here, d_f^T and d_m^T denote the damage variable of the fiber and matrix tensile failure, respectively. ϵ_f^{0T} and ϵ_m^{0T} are the tensile strain for damage initiation. ϵ_f^{fT} and ϵ_m^{fT} denote the tensile strain at final failure.

The failure initiation tensile strain and the final failure tensile strain are given by the following equations:

$$\begin{aligned}
 \epsilon_f^{0T} &= \frac{X^T}{E_1} \\
 \epsilon_m^{0T} &= \frac{Y^T}{E_2} \\
 \epsilon_f^{fT} &= \frac{2G_{1C}^T}{X^T l^*} \\
 \epsilon_m^{fT} &= \frac{2G_{2C}^T}{Y^T l^*}
 \end{aligned}
 \tag{12}$$

where E_1 and E_2 are the elastic modulus in the longitudinal direction and transverse direction, respectively. G_{1C}^T and G_{2C}^T denote the fracture energy associated with fiber and matrix tensile failure, respectively. l^* is the characteristic length which would ensure a constant energy release rate per unit area of crack and make the results independent of mesh size.

Similarly, the compressive damage variable d_f^C in the fiber direction can be expressed:

$$d_f^C = \frac{\epsilon_f^{fC}}{\epsilon_f^{fC} - \epsilon_f^{0C}} \left(1 - \frac{\epsilon_f^{0C}}{\epsilon_f} \right)
 \tag{13}$$

where ϵ_f^{0C} is the compressive strain for damage initiation and ϵ_f^{fC} denotes the compressive strain at final failure.

The strain at failure initiation and at final failure are obtained by a similar approach.

$$\begin{aligned}
 \epsilon_f^{0C} &= \frac{X^C}{E_1} \\
 \epsilon_f^{fC} &= \frac{2G_{1C}^C}{X^C l^*}
 \end{aligned}
 \tag{14}$$

Here, G_{1C}^C denotes the fracture energy associated with fiber compressive failure.

For matrix compressive failure, the compressive damage variable d_m^C is a function of strain form.

$$d_m^C = \frac{\gamma_{mat}^{fC}}{\gamma_{mat}^{fC} - \gamma_{mat}^{0C}} \left(1 - \frac{\gamma_{mat}^{0C}}{\gamma_{mat}} \right) \tag{15}$$

where γ_{mat} is the shear strain on the fracture plane is defined as:

$$\gamma_{mat} = \sqrt{\gamma_{nt}^2 + \gamma_{nl}^2} \tag{16}$$

Here, γ_{nt} and γ_{nl} are the strain rotated to the fracture plane and given by:

$$\begin{aligned} \gamma_{nt} &= \varepsilon_{33} \sin \theta \cos \theta + \gamma_{23} (\cos^2 \theta - \sin^2 \theta) - \varepsilon_{22} \sin \theta \cos \theta \\ \gamma_{nl} &= \gamma_{12} \sin \theta + \gamma_{13} \cos \theta \end{aligned} \tag{17}$$

where ε_{22} , ε_{33} , γ_{12} , γ_{13} , γ_{23} represent the effective strain components.

The γ_{mat}^{0C} is the failure onset strain and is recorded by the program once the damage initiation criterion Eq. (7) for matrix compressive failure has been satisfied. The final failure strain γ_{mat}^{fC} is defined in terms of the fracture energy for matrix compressive failure G_{2C}^C , the damage initiation stress τ_{mat}^{0C} and the characteristic length l^* :

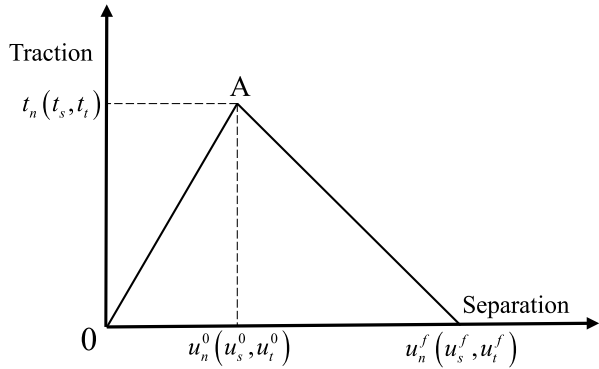
$$\gamma_{mat}^{fC} = \frac{2G_{2C}^C}{\tau_{mat}^{0C} l^*} \tag{18}$$

The material damage model of the EHM is implemented into Abaqus/Explicit by a user-defined material subroutine (VUMAT), and the element deletion during the simulation is controlled by a state variable defined in the VUMAT. The material parameters are obtained through consulting manufacturers and some values are extracted from the literature by referring comparable CFRPs with similar mechanical performance. as shown in Table 1 [24, 34].

Table 1 Material properties of EHM

Properties	Value
E_1 (GPa)	178
$E_2 = E_3$ (GPa)	9.5
$G_{12} = G_{13}$ (GPa)	6.33
G_{23} (GPa)	4.21
$\nu_{12} = \nu_{13}$	0.29
ν_{23}	0.37
X^T (MPa)	2980
X^C (MPa)	1450
Y^T (MPa)	110
Y^C (MPa)	350
S (MPa)	90
ρ (g/cm ³)	1.53
G_{1C}^T (N/mm)	91.6
G_{1C}^C (N/mm)	79.9
G_{2C}^T (N/mm)	0.22
G_{2C}^C (N/mm)	2

Fig. 9 Traction–separation response



The material behavior of the cohesive element follows a typical bilinear traction–separation response, as shown in Fig. 9. The quadratic nominal stress criterion is used for the prediction of the damage onset [18, 23, 24]:

The damage initiation condition has the following form:

$$\left\{ \frac{t_n}{t_n^0} \right\}^2 + \left\{ \frac{t_s}{t_s^0} \right\}^2 + \left\{ \frac{t_t}{t_t^0} \right\}^2 = 1 \tag{19}$$

where n represents the normal direction, s and t represent the first and second shear direction respectively, as shown in Fig. 10. t_n , t_s and t_t are the instantaneous components of the normal and shear tractions, while t_n^0 , t_s^0 , t_t^0 are the peak values of the normal and shear tractions.

Once the damage initiation condition is fulfilled, the cohesive element stiffness begins to degrade linearly linked to damage variable D given by equation:

$$D = \frac{u_m^f(u_m - u_m^0)}{u_m(u_m^f - u_m^0)} \tag{20}$$

Here, u_m^0 and u_m^f represent the displacement at damage initiation and complete failure, respectively. The u_m parameter corresponds to the total displacement given by:

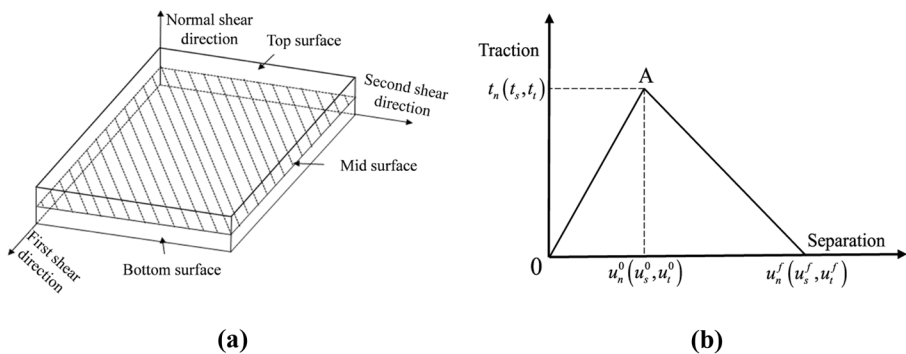


Fig. 10 Cohesive element: (a) Schematic diagram of the cohesive element; (b) Directions of the cohesive element

Table 2 Material properties of the cohesive elements

Type	t_n^0 (MPa)	t_s^0 (MPa)	t_t^0 (MPa)	G_n^C (N/mm)	G_s^C (N/mm)	G_t^C (N/mm)
Intralaminar	82	40	40	0.22	0.7	0.7
Interlaminar	60	110	110	0.33	1.209	1.209

$$u_m = \sqrt{u_n^2 + u_s^2 + u_t^2} \tag{21}$$

where u_n is the displacement of the normal direction, u_s and u_t represent the displacement of the first and second shear direction respectively.

The cohesive element fails when the energy absorbed meets the power law criterion.

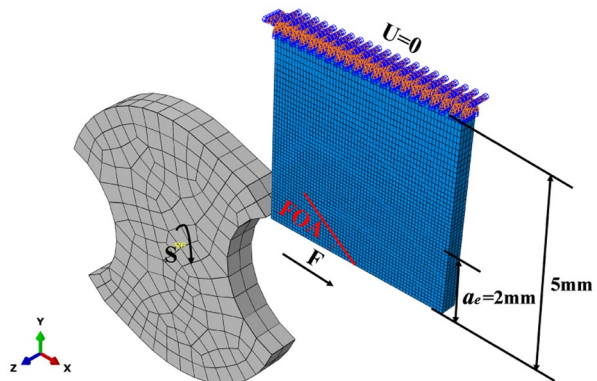
$$\left\{ \frac{G_n}{G_n^C} \right\}^\alpha + \left\{ \frac{G_s}{G_s^C} \right\}^\alpha + \left\{ \frac{G_t}{G_t^C} \right\}^\alpha = 1 \tag{22}$$

where G_n , G_s and G_t denote the instantaneous fracture energies in normal, first, and second shear directions, respectively. While G_n^C , G_s^C , G_t^C refer to the critical fracture energies in three directions. α is material properties determined by experiment, $\alpha = 1.6$ [35]. The material properties of the cohesive element are listed in Table 2 [24, 35].

2.3 Geometric Model and Boundary Conditions

The FE model is developed according to the experimental setup. In order to improve the computational efficiency, a portion of the workpiece material is modeled. The hang-out distance of the workpiece in the simulation (Fig. 11) and experiment is 5 mm to guarantee the same boundary conditions. The dimension of the workpiece is $6 \times 6 \times 0.5$ mm and the thickness of each layer is 0.125 mm. The calculation accuracy and efficiency should be considered when setting the mesh size. According to the simulation tests, the results with the highest accuracy were acquired when the mesh size was 100 μm , and there were no significant changes in the result accuracies when using mesh sizes less than 100 μm . Concurrently, in order to avoid the influence of different mesh sizes on

Fig. 11 Milling simulation model



surface damage, the geometric models of the top layer are set to the uniform mesh size of 100 μm . Furthermore, the geometric models of the other three layers are meshed with the element size of 100 μm in the cutting zone while a relatively coarse mesh is applied in the area away from the cutting zone. The insert interval of cohesive elements is determined from experiments for computing efficiency. The optimized insert interval of the cohesive elements in the top layer of the four typical FOAs CFRPs is set to 100 μm . The mill cutter is modeled as a rigid body. The 4-node linear tetrahedron elements without element deletion (C3D4) are defined for the mill cutter, and the element size is set to 500 μm .

Friction is an important factor that influences the cutting forces in machining simulation. Coulomb friction model is used to simulate the frictional effect between the tool and workpiece. The friction coefficient between the tool and the composite material is dependent on the FOA, and it is determined as 0.3, 0.6, 0.8, and 0.6 for 0° , 45° , 90° , and 135° FOAs, respectively [36–38]. In order to avoid the element distortion, a general contact is used in this simulation. The side of the workpiece is clamped by fixing all the degrees of freedom of the nodes. The mill cutter is constrained in the Y and Z directions, which allows to move along the X axis and rotate along the Z axis, as shown in Fig. 11. The feed rate and spindle speed are 600 mm/min and 3000 rpm, respectively. The cutting depth (a_e) is 2 mm.

3 Experimental Setup

The UD-CFRP laminates employed in the experiment was made from P2352 prepreps with T800S fibers and 3900-2B epoxy resin (Toray Ltd, Tokyo, Japan). The workpiece was cut into four typical FOAs including 0° , 45° , 90° , and 135° , and the dimension was $50 \times 50 \times 3$ mm. A polycrystalline diamond (PCD) cutter was used in this work, which exhibited a double-straight cutting edge with a diameter of 10 mm. The geometric parameters of the mill cutter are shown in Table 3.

The milling process was performed on a high-speed milling machine (HSM500, Mikron, Agno, Switzerland), as shown in Fig. 12a. Processing parameters were determined based on the simulation. The milling forces were measured by a dynamometer (9327C, Kistler, Winterthur, Switzerland) with a charge amplifier (5073A, Kistler, Winterthur, Switzerland) and a data acquisition device (5697A, Kistler, Winterthur, Switzerland). The milling force signals were collected and analyzed using the commercial software DynoWare (Kistler, Winterthur, Switzerland), as shown in Fig. 12b. The charge amplifier converted the induced signals, which were proportional to the applied force, to voltage and the voltage signals were recorded through the data acquisition system. The resulting signals were converted to the milling force by the calibrated data in the software. Measurements were obtained with a frequency of 6000 Hz and the accuracy of 0.2 N in milling process. The workpiece was firmly fixed onto the dynamometer using four bolts. A high accuracy digital microscope (VHX-600E) was also used to observe the damage induced on the machined surface.

Table 3 The geometric parameters of the mill cutter

Rake angle	Relief angle	Diameter	The length of cutting edge	Cutting edge radius
5°	10°	10 mm	20 mm	5 μm

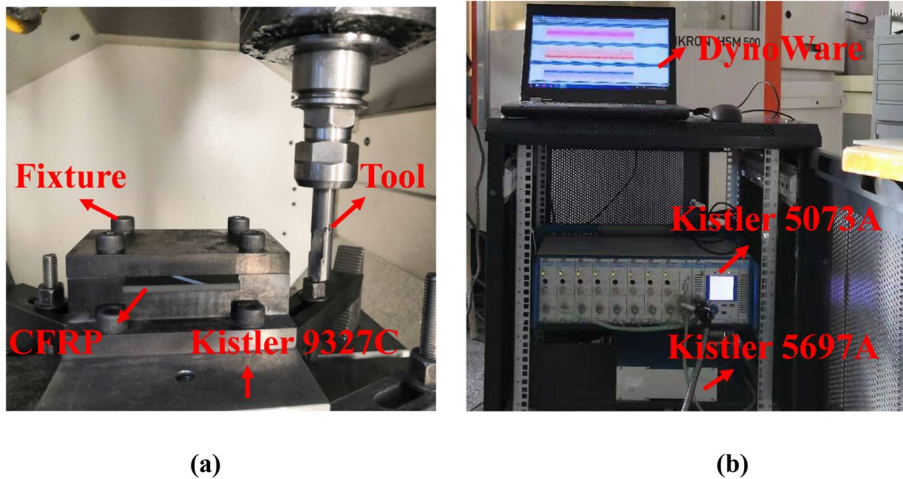


Fig. 12 Experimental setup: **(a)** The experimental platform; **(b)** The force measurement system

4 Results and Discussions

The cutting forces, burr and tear damages at the four typical FOAs are obtained by the simulation, and the predicted results are verified through the comparison with the experimental outputs. In addition, the formation process of the burr and tear at the four typical FOAs is analyzed.

4.1 Cutting Forces

The cutting forces are an important factor affecting the surface damages of the CFRPs, which can be predicted with the help of FE models. In order to verify the FE models, the periodic curve of the cutting forces at the four typical FOAs acquired through experiments and simulations are recorded. Since the thickness of the workpiece in the FE model and experiment is 0.5 mm and 3 mm respectively, the cutting forces cannot be compared directly. In this case, the cutting force per unit thickness is calculated for the validation. Namely, the cutting force per unit thickness is obtained by dividing the cutting force value by total thickness. The experimental and simulation results are shown in Fig. 13. Wherein the F_x is the cutting force while F_y is the thrust force.

Due to the cutting forces are periodic, the average value of the cutting force peak is compared between the experimental and simulation results, as shown in Fig. 14. Experimental and FE results show the change trend of the experimental and simulation cutting forces per unit thickness is consistent. The overall simulation results are generally smaller than the experimental results. The errors can be attributed to that though the material stiffness degradation model is set up in progressive damage model, the element stiffness degradation follows the linear damage evolution laws. When the element reaches the failure strength, it will no longer bear force and be deleted automatically. But in the actual cutting process, the material damage is not synchronous and irregular, which creates the irregular

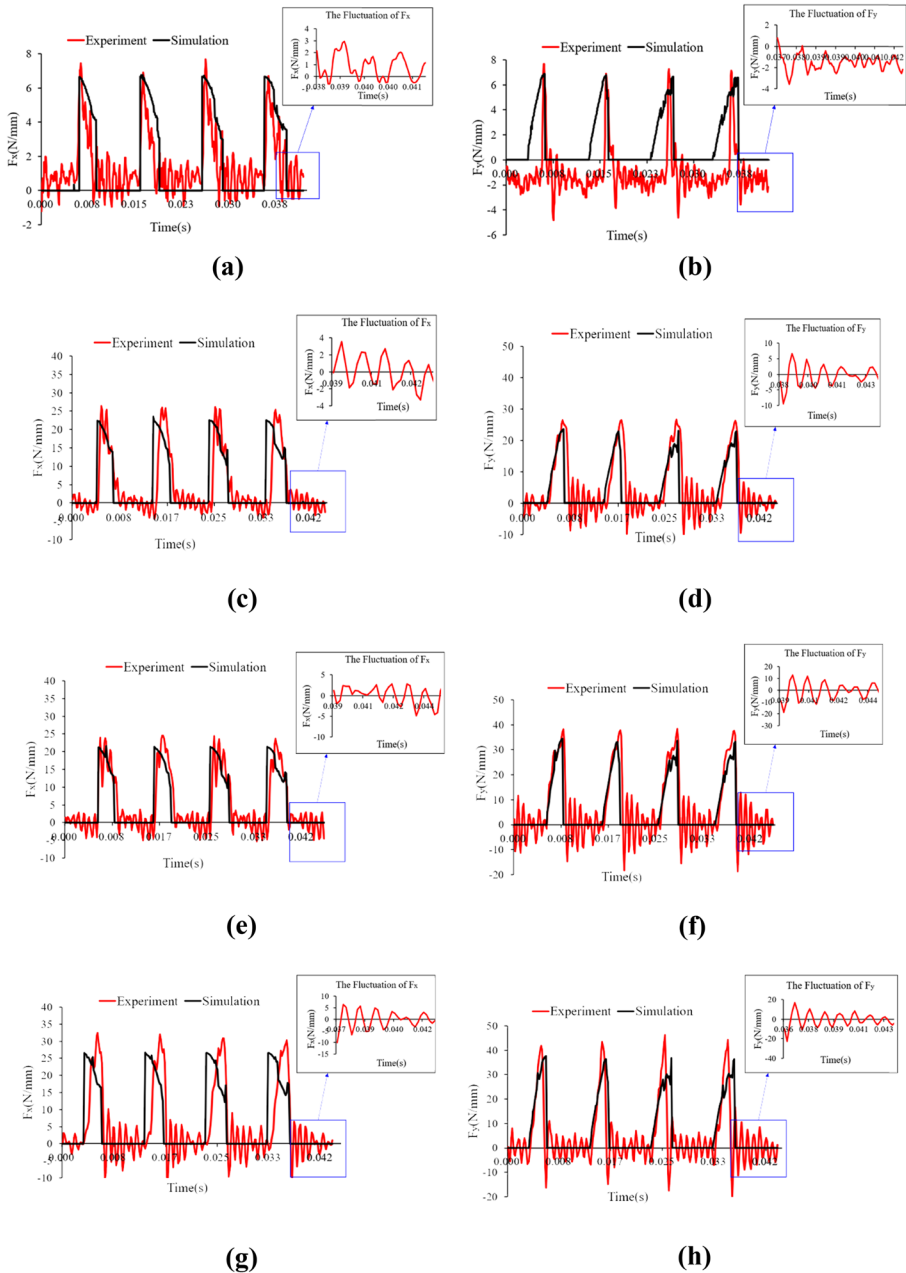


Fig. 13 The curve of the cutting forces per unit thickness under the four typical FOAs: **(a)** F_x at 0° FOA; **(b)** F_y at 0° FOA; **(c)** F_x at 45° FOA; **(d)** F_y at 45° FOA; **(e)** F_x at 90° FOA; **(f)** F_y at 90° FOA; **(g)** F_x at 135° FOA; **(h)** F_y at 135° FOA

degradation of material properties. When chips are formed, some chips continue to remain in the fiber bundles and bear force. Besides, In the experiment, the removal process of CFRPs becomes more difficult with the increase of the FOA, which results in a larger fluctuation of cutting forces.

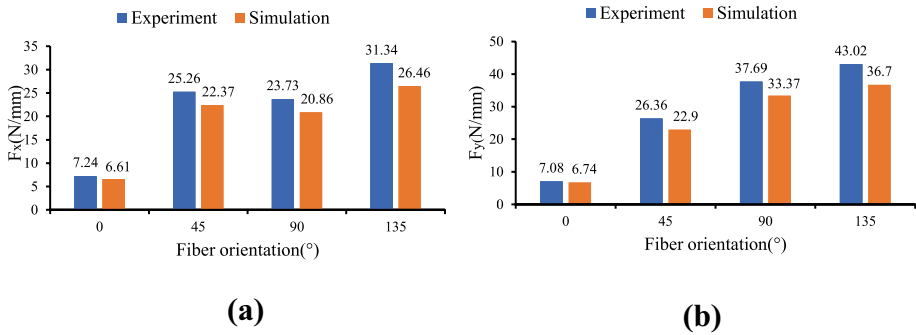


Fig. 14 Simulation and experimental cutting forces per unit thickness under the four typical FOAs: (a) F_x ; (b) F_y

tuation of the cutting force (Fig. 13) and increases the peak value of the cutting force. However, CFRPs are modeled as an equivalent homogeneous material in the simulation, the fluctuation of the cutting force is small. Thus, the relative deviation is the maximum when milling 135° FOA CFRPs, and the value is 15.3%. It could be considered that the simulation results are in good agreement with the experimental value. In addition, the errors have little impact on the research of surface damages under different FOA.

As can be seen, F_y rises with the increase of the FOA. F_x acquires its minimum and maximum values at the 0° and 135° FOAs respectively, and there is no significant difference when cutting 45° and 90° FOAs CFRPs. In the milling of the 0° FOA CFRPs, the workpiece is lifted and the chips are removed due to the intralaminar cracking. As the strength of the interface is far less than that of the fibers, thus the cutting force is the lowest because the material is removed not by the direct cutting of the fibers. When milling 45° FOA CFRPs, the CFRPs are mainly subjected to the shear action of the tool. Since the shear strength of the CFRPs is low, the cutting force of the 45° FOA CFRPs is small. Regarding the 90° FOA CFRPs, the fibers are perpendicular to the feed direction, thus the material is removed mainly due to the shear failure. Meanwhile, the cracks propagate along the fiber direction into the machined surface, and the fibers fracture under the machined surface. Therefore, the cutting forces are large. In the milling of the 135° FOA CFRPs, more cracks propagate into the processed surface. The fibers would be lifted and form significant deformation under the bending pressure of the tool. Thus, the material is removed mainly due to the bending fracture. Since the tensile strength of the fibers is far larger than the shear strength of the CFRPs, the cutting force obtained its maximum value.

4.2 Analysis of the Surface Damage at the Four Typical FOAs

When milling 0° FOA CFRPs, the feed direction of the mill cutter is parallel to the fiber direction. The workpiece in the cutting area is deformed by the extrusion of the tool, which results in the cutting force F_x and the thrust force F_y . In order to analyze the effect of cutting force on damage, the cutting force is decomposed into the force F_1 along the fiber direction and the force F_2 perpendicular to the fiber direction, as shown in Fig. 15a. With the feed and rotation of the tool, the cutting forces increase gradually. Because the strength of the cohesive elements is far less than that of the EHM, the cohesive elements fail, which leads

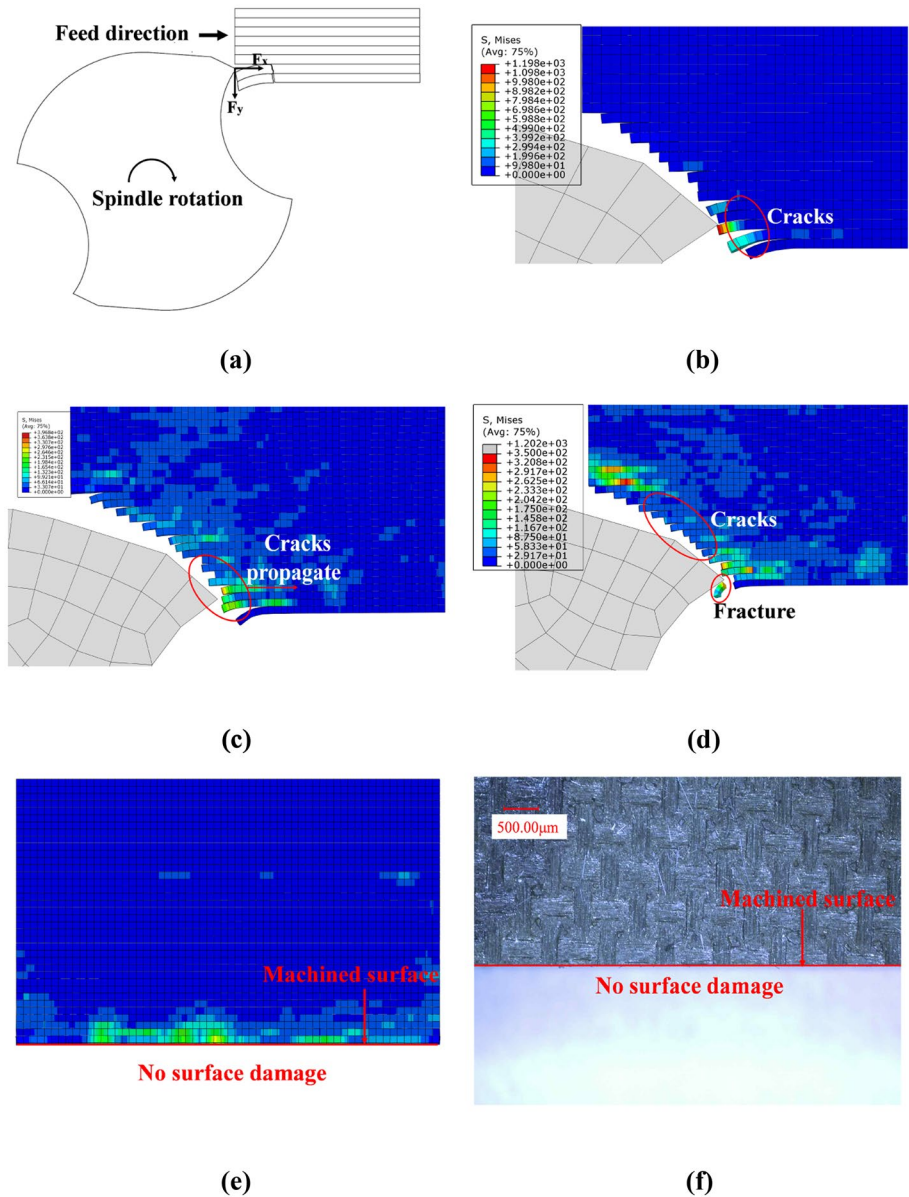


Fig. 15 Analysis of the surface damage at 0° FOA CFRPs: (a) Schematic diagram of F_1 and F_2 ; (b) Formation of cracks; (c) Propagation of cracks; (d) CFRPs fracture; (e) Machined surface of simulation; (f) Machined surface of experiment

to the formation of crack. At the meantime, the cracks propagate along the fiber direction and material is lifted, in addition, the cutting stress is mainly concentrated near the tool tip, as shown in Fig. 15b. As the mill cutter moves continuously, the cracks keep expanding and the deformation of the material enhances, moreover, the cutting stress extends to uncut material zone along the fiber direction, as shown in Fig. 15c. When the stress exceeds the

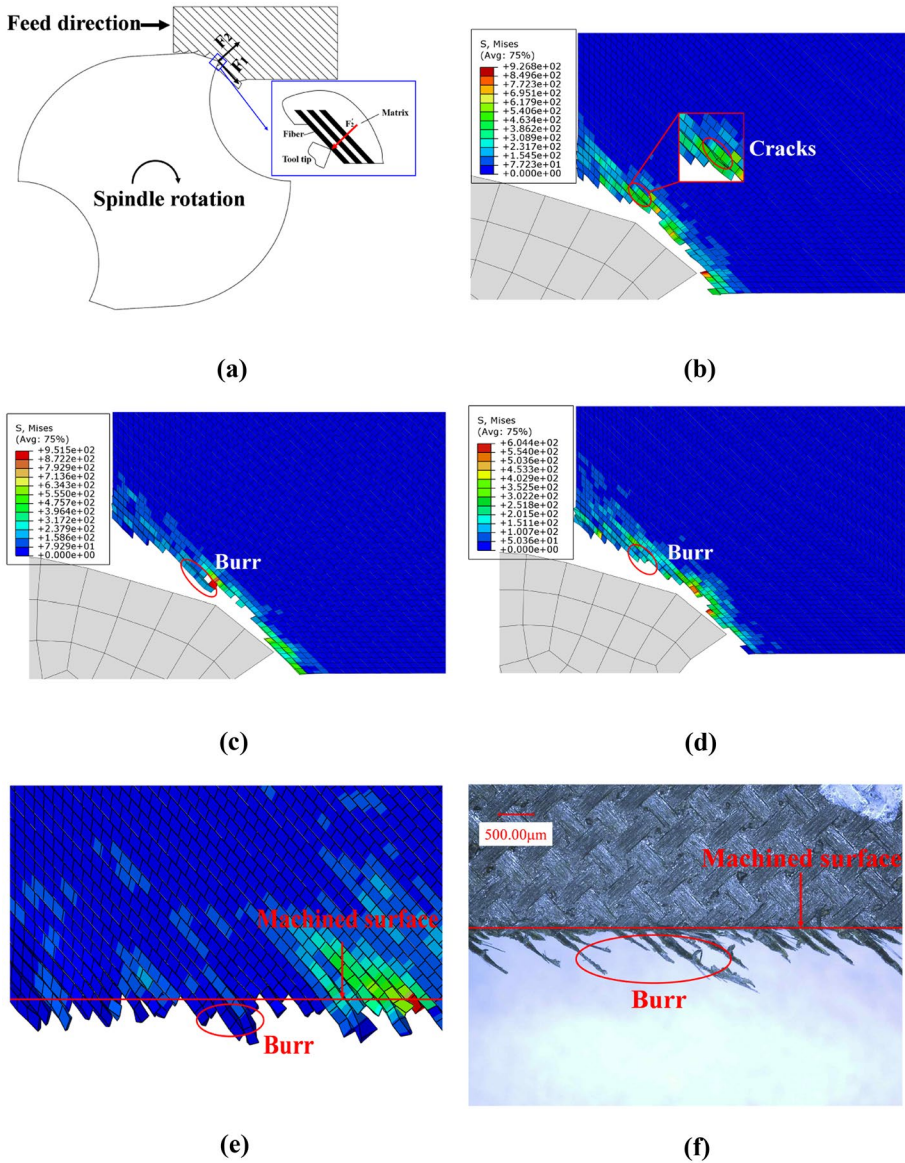


Fig. 16 Analysis of the surface damage at 45° FOA CFRPs: (a) Schematic diagram of F_1 and F_2 ; (b) Formation of cracks; (c) Long burr; (d) Short burr; (e) Machined surface of simulation; (f) Machined surface of experiment

strength limit of the CFRPs, the material in the cutting area fractures, as shown in Fig. 15d. There are stress concentration areas near the machined surface, which are caused by the stress of the materials under the extrusion of the tool, as shown in Fig. 15e. Due to the crack propagation and the fracture of the CFRPs occurs in the cutting zone, the damage is removed. The quality of the machined surface is well, and there are no burrs and tears left. The simulation results (Fig. 15e) are consistent with the experimental results (Fig. 15f).

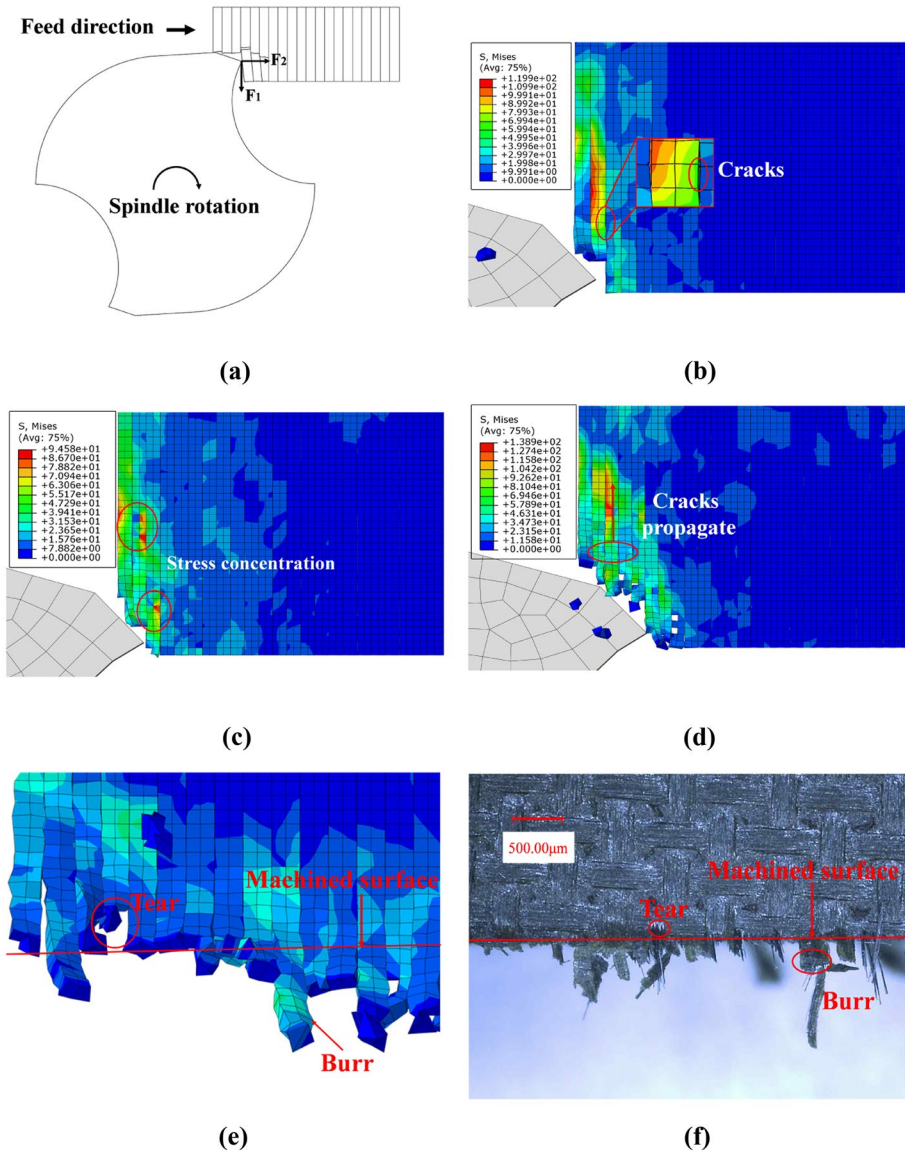


Fig. 17 Analysis of the surface damage at 90° FOA CFRPs: (a) Schematic diagram of F_1 and F_2 ; (b) Formation of cracks; (c) Stress concentration; (d) Propagation of cracks; (e) Machined surface of simulation; (f) Machined surface of experiment

Regarding the cutting of 45° FOA CFRPs, the angle between feed direction and fiber direction is an acute angle, as shown in Fig. 16a. With the movement of the tool, the cutting forces cause the failure of the cohesive elements. Then, the cracks form and extend along the fiber direction, as shown in Fig. 16b, meanwhile, the stress mostly concentrates in the cutting material zone. Owing to the cutting force F_2 towards the internal of the workpiece, the deformation of the CFRPs in the cutting area is small due to the supporting force

F_2' of the workpiece on the CFRPs in the cutting zone is large. Since the fibers are mainly subjected to the shear action of the tool, while the low shear strength of the fibers, it is easy to be cut off directly. What's more, uncut fibers remain above the machined surface and form burrs due to the shear failure in the machining area under the combined action of the cutting forces F_1 and F_2 . With the mill cutter moves continuously, the length of the burr is reduced due to the fracture of the CFRPs, as shown in Fig. 16c-e. Because the fibers bear the tensile stress caused by the tensile force F_1 during processing, there are also stress con-

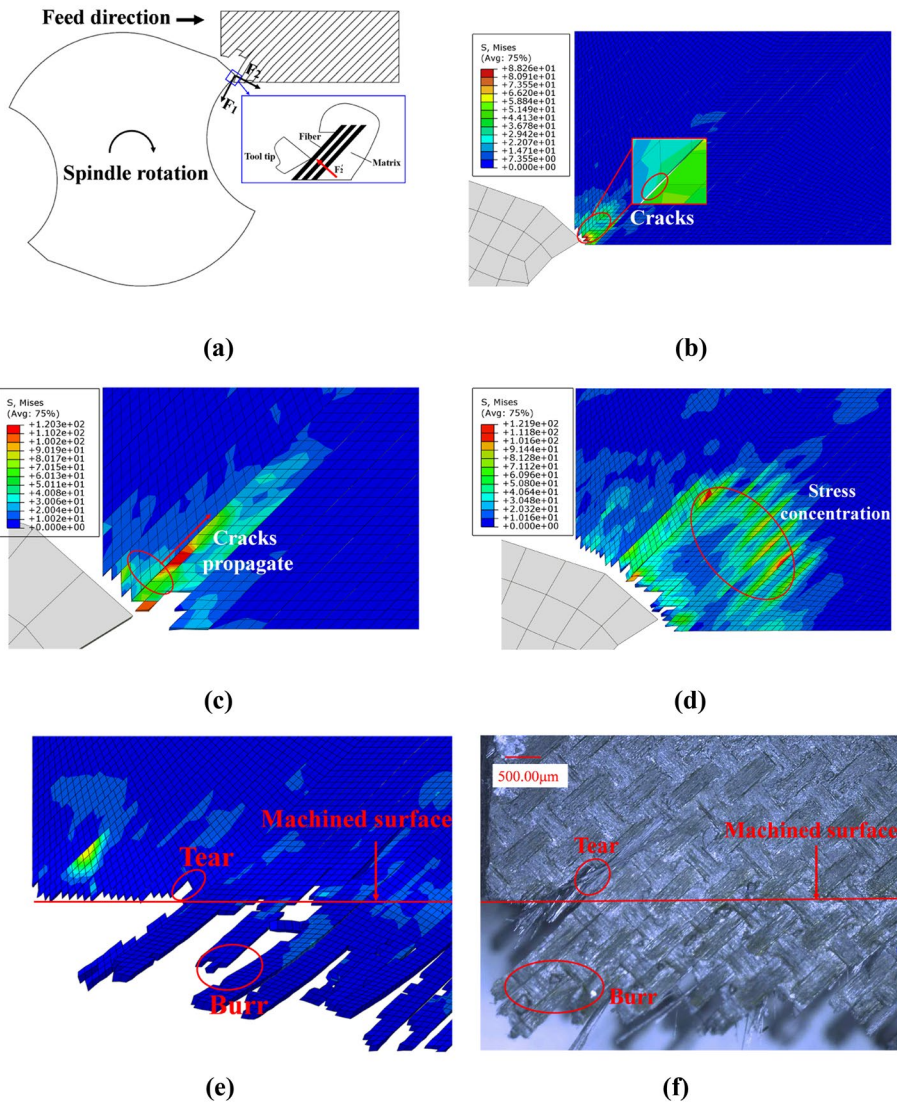


Fig. 18 Analysis of the surface damage at 135° FOA CFRPs: (a) Schematic diagram of F_1 and F_2 ; (b) Formation of cracks; (c) Propagation of cracks; (d) Cracks propagate into the processed surface; (e) Machined surface of simulation; (f) Machined surface of experiment

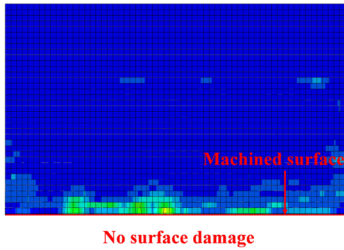
Fig. 19 The length of the burr in experiment and simulation: (a) Simulation results of 0° FOA CFRPs; (b) Experimental results of 0° FOA CFRPs; (c) Simulation results of 45° FOA CFRPs; (d) Experimental results of 45° FOA CFRPs; (e) Simulation results of 90° FOA CFRPs; (f) Experimental results of 90° FOA CFRPs; (g) Simulation results of 135° FOA CFRPs; (h) Experimental results of 135° FOA CFRPs; (i) The length of the burr; (j) Relative errors

centration areas near the processed surface, as shown in Fig. 16e. The simulation (Fig. 16e) and experimental results (Fig. 16f) both show that there are significant burrs when milling 45° FOA CFRPs.

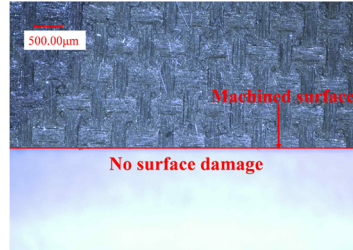
When cutting 90° FOA CFRPs, the feed direction of the mill cutter is perpendicular to the fiber direction, as shown in Fig. 17a. With the movement of the mill cutter, the increased cutting forces cause the failure of the cohesive elements, and the cracks form. Furthermore, the fibers are subjected to the tensile stress and shear stress under the cutting and extrusion of the tool. Since the cracks propagate along the fiber direction into the unprocessed material zone, the material is lifted and the deformation is increased, moreover, the stress mostly distributes around the tool tip and the uncut material area. As the tensile strength of the fibers is far exceeding the shear strength, the fibers in the cutting area would be easily fractured owing to the shear failure under the effect of the cutting forces F_2 . Due to the fibers bear tensile stress, part of the fibers would break when the tensile strength is overcome. The maximum stress is at the tensile stress concentration point in the unprocessed material zone and the uncertainty of the tensile stress concentration position, thus the fibers fracture above or below the machined surface, and form burr or tear respectively, as shown in Fig. 17b–e. The simulation (Fig. 17e) and experimental results (Fig. 17f) show that there are burrs and tears in the machined top layer of the 90° FOA CFRPs.

When milling 135° FOA CFRPs, the feed direction and the fiber direction is at an obtuse angle, as shown in Fig. 18a. Since the force F_2 towards the external of the workpiece, the CFRPs in the cutting area are more prone to deformation due to the supporting force F'_2 of the workpiece on the CFRPs in the cutting zone is small. Thus, the cracks are more susceptible to form by the failure of the cohesive elements and expand into the unprocessed surface, in addition, there are stress concentration zones at the tool tip and near the maximum bending stress concentration point in the uncut material area. With the mill cutter continues to move, more cracks are generated in the cutting zone and they propagate into the processed surface. Concurrently, the bending stress of the CFRPs enlarges gradually and extends to the unprocessed material zone along the fiber direction, moreover, the cutting stress mainly concentrates in the uncut CFRPs region, and the stress range is large. Moreover, the CFRPs are lifted and form significant deformation, thus long burrs are formed. The material breaks when the stress reaches the strength limit under the combined action of the cutting forces F_1 and F_2 . Due to the unpredictability of the bending stress concentration position, the fracture position occurs above and below the processed surface, resulting in the tear and burr, as shown in Fig. 18b–e. The simulation (Fig. 18e) and experimental results (Fig. 18f) show that the top layer of 135° FOA CFRPs has serious burr and tear.

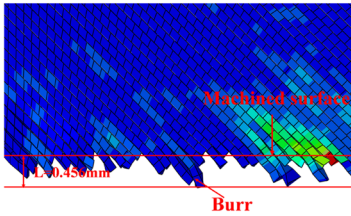
It can also be acquired from Fig. 15–18 that the surface damages become more serious with the increase of the FOA. 0° CFRP has the good machined surface quality, there is burr damage when FOAs are 45°, 90° and 135°, moreover, 90° CFRP and 135° CFRP have tear damage. Besides, in order to quantitatively assess the burr at the four typical FOAs, the length of the burr obtained in the experiments and simulations is compared. Namely, the distance from the uncut fibers to the machined surface. The results of the experiments and simulations are shown in Fig. 19.



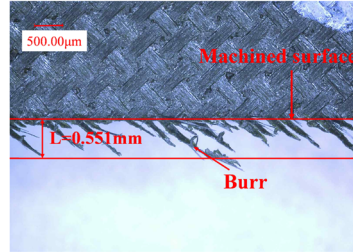
(a)



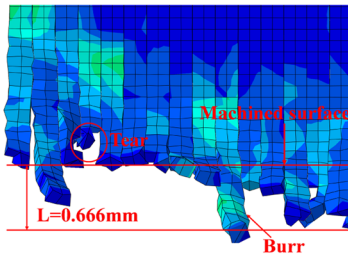
(b)



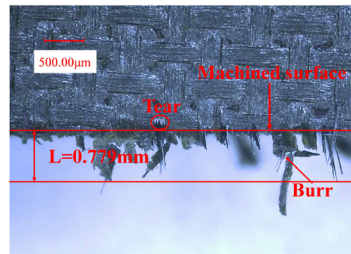
(c)



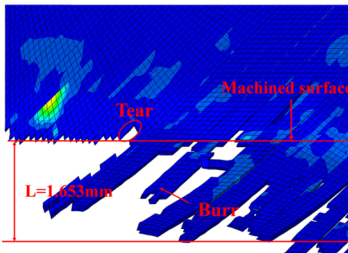
(d)



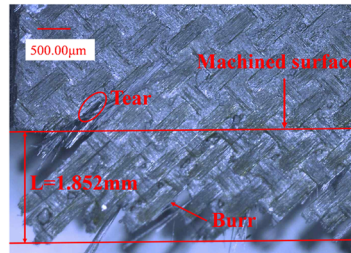
(e)



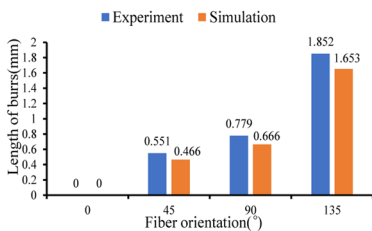
(f)



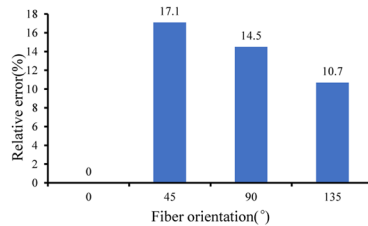
(g)



(h)



(i)



(j)

It can be seen from Fig. 19 that the average length of the burr becomes longer with the increase of the FOA. The damage is removed in the cutting zone during the cutting of 0° FOA CFRPs, thus there is no burr. When cutting 45° FOA CFRPs, the deformation of the material is small due to the supporting effect of the workpiece on the CFRPs in the cutting zone is strong, therefore, the length of the burr is short. During the milling of the 90° FOA CFRPs, the workpiece is lifted and large deformation of the material is caused, so the burr length is long. The 135° FOA CFRPs are more susceptible to deform due to the supporting effect of the workpiece on the CFRPs in the cutting zone is weak, so the burr length is significant long. The maximum relative error of the burr length between the simulation and experimental results is 17.1%, which is acceptable. In the experiment, due to the intralaminar cracking in the top layer, the fibers could withstand great deformation and form long burr. In the simulation, the workpiece is modeled as EHM, when the stress exceeds the strength limit of the CFRPs, the elements would be deleted after failure, which causes EHM to form short burr. In addition, the CFRPs are more prone to form significant deformation due to the cracks are more susceptible to form and expand into the unprocessed surface with the increase of the FOA in the simulation, so the relative error decreases with the increase of FOA.

5 Conclusions

In this paper, a 3D FE model is proposed to reveal the formation mechanism of the burr and tear during the milling of CFRP laminates. The intralaminar cracking is simulated by inserting cohesive elements in the top layer along the fiber direction, and the cohesive elements are also applied to model the interlaminar fracture. A Python script for developing the model is defined to realize parametric modeling of the CFRP milling thus increase the modeling efficiency. The cutting forces and the extents of the burr and tear at four typical FOAs are thoroughly analyzed. The conclusions are as follows.

- (1) FOA has a significant impact on cutting force, and surface damage in CFRP milling. The cutting force follows that F_y rises with the increase of the FOA. F_x acquires its minimum and maximum values at the 0° and 135° FOAs respectively. When FOA is 0° , the failure of the interface is the main cause of the material removal, so the cutting forces are the minimum. For 45° CFRP, as CFRP is subjected to shear failure, the cutting forces are small. When FOA is 90° , the material is removed mainly due to the shear failure, hence there is no big difference between the cutting force F_x of 90° and 45° CFRP. Since part of the fibers would break when the tensile strength is overcome, the cutting force F_y is large. Regarding 135° CFRP, the fibers fracture mainly due to the bending stress, so the cutting forces are the maximum.
- (2) From the results, the average length of the burr becomes longer with the increase of the FOA. When FOA is 0° , the fracture of the CFRP occurs in the cutting zone and the damage is removed, thus there is no burr. For 45° , 90° and 135° CFRP, the cracks caused by failed cohesive elements propagate along the fiber direction into the unprocessed zone, so the fibers are more prone to deformation, which prevent them from being completely cut off, uncut fibers remained above the machined surface form burr. Since the cutting force F_2 perpendicular to the fiber direction towards the internal and external of the workpiece at the 45° and 135° FOAs respectively, the deformation of 45° CFRP in the cutting area is small due to the strong supporting effect while the 135°

CFRP is more prone to deformation owing to the weak supporting effect. Thus, the burr length of 45° CFRP is short and 135° CFRP has significant long burr.

- (3) In this research, 90° and 135° CFRP have significant tear damage. The stress extends to machined surface along the fiber direction, resulting in the unpredictability of the stress concentration position. The CFRP fractures below the machined region and forms tear. Due to the material is lifted and forms significant deformation under the bending stress at the 135° FOA, more cracks propagate into the processed surface, so the fibers are more prone to fracture below the processed region, which cause serious tear. Therefore, 0° CFRP has the good machined surface quality, 45° CFRP has relatively machined surface quality and burr damage, 90° and 135° CFRP have a poor surface quality, with burr and tear damage.

The proposed model can be used to simulate the surface damage during the milling of CFRPs and the formation mechanisms of the surface damage are revealed. The findings are expected to be the crucial theoretical guidance for the suppression of the surface damage.

Acknowledgements This work is supported by National Key R&D Program of China (Grant No. 2018YFA0702803); Liaoning Revitalization Talents Program (Grant No. XLYC1902014, XLYC1801008 and XLYCYSZX1901). The authors wish to thank the anonymous reviewers for their comments which lead to improvements of this paper.

Data Availability Statement The datasets generated during the current study are available from the corresponding author on reasonable request.

References

1. Qi, Z., Zhang, K., Cheng, H.: Microscopic mechanism based force prediction in orthogonal cutting of unidirectional CFRP. *Int. J. Adv. Manuf. Technol.* **79**, 1209–1219 (2015)
2. Li, H., Qin, X., He, G.: Investigation of chip formation and fracture toughness in orthogonal cutting of UD-CFRP. *Int. J. Adv. Manuf. Technol.* **82**, 1079–1088 (2016)
3. Lin, Y.: Analysis Model and Numerical Simulation of Thermoelectric Response of CFRP Composites. *Appl. Compos. Mater.* **26**, 435–454 (2018)
4. Prentzias, V., Tsamasphyros, G.J.: Simulation of Low Velocity Impact on CFRP Aerospace Structures: Simplified Approaches, Numerical and Experimental Results. *Appl. Compos. Mater.* **26**, 835–856 (2018)
5. Qin, X., He, G., Jin, Y.: Investigation of chip formation and fracture toughness in orthogonal cutting of UD-CFRP. *Int. J. Adv. Manuf. Technol.* **82**, 1079–1088 (2016)
6. Ning, F., Cong, W., Wang, H.: Surface grinding of CFRP composites with rotary ultrasonic machining: a mechanistic model on cutting force in the feed direction. *Int. J. Adv. Manuf. Technol.* **92**, 1217–1229 (2017)
7. Li, H., Qin, X., Huang, T.: Machining quality and cutting force signal analysis in UD-CFRP milling under different fiber orientation. *Int. J. Adv. Manuf. Technol.* **98**, 2377–2387 (2018)
8. Su, F., Yuan, J., Sun, F., Wang, Z., Deng, Z.: Analytical cutting model for a single fiber to investigate the occurrences of the surface damages in milling of CFRP. *Int. J. Adv. Manuf. Technol.* **96**, 2671–2685 (2018)
9. Chen, Y., Guo, X., Zhang, K.: Study on the surface quality of CFRP machined by micro-textured milling tools. *J. Manuf. Process.* **37**(1), 114–123 (2019)
10. Wang, F., Yin, J., Ma, J., Jia, Z., Yang, F., Niu, B.: Effects of cutting edge radius and fiber cutting angle on the cutting-induced surface damage in machining of unidirectional CFRP composites laminates. *Int. J. Adv. Manuf. Technol.* **91**, 3107–3120 (2017)
11. Colligan, K., Ramulu, M.: The effect of edge trimming on composite surface plies. *Manuf. Rev.* **5**(4), 274–283 (1992)
12. Hintze, W., Cordes, M., Koerkel, G.: Influence of weave structure on delamination when milling CFRP. *J. Mater. Process. Technol.* **216**, 199–205 (2015)

13. Haddad, M., Zitoune, R., Bougherara, H.: Study of trimming damages of CFRP structures in function of the machining processes and their impact on the mechanical behavior. *Compos. B.* **57**, 136–143 (2014)
14. Wang, F., Wang, X., Yang, R.: Research on the carbon fibre-reinforced plastic (CFRP) cutting mechanism using macroscopic and microscopic numerical simulations. *J. Reinf. Plast. Compos.* **36**, 555–562 (2016)
15. Hassouna, A., Mzali, S., Zemzemi, F.: Orthogonal cutting of UD-CFRP using multiscale analysis: Finite element modeling. *J. Compos. Mater.* **1**, 1–14 (2020)
16. Liu, H., Lin, J., Sun, Y.: Micro Model of Carbon Fiber/Cyanate Ester Composites and Analysis of Machining Damage Mechanism. *Chin. J. Mech. Eng-en.* **32**(1), 1–11 (2019)
17. Zhang, L., Wang, S., Qiao, W.: High-speed milling of CFRP composites: a progressive damage model of cutting force. *Int. J. Adv. Manuf. Tech.* **106**(3), 1005–1015 (2020)
18. Phadnis, V.A., Makhdam, F., Roy, A., Silberschmidt, V.V.: Drilling in carbon/epoxy composites: Experimental investigations and finite element implementation. *Compos. Part. A-Apl. S.* **47**, 41–51 (2013)
19. Isbilir, O., Ghassemieh, E.: Numerical investigation of the effects of drill geometry on drilling induced delamination of carbon fiber reinforced composites. *Compos. Struct.* **105**, 126–133 (2013)
20. Feito, N., Diaz, Álvarez, J., López, Puente, J., Miguelez, M.H.: Numerical analysis of the influence of tool wear and special cutting geometry when drilling woven CFRPs. *Compos. Struct.* **138**, 285–94 (2016)
21. He, Y., Liu, Y., Gao, J.: Macro and Micro Models of Milling of Carbon Fiber Reinforced Plastics Using Fem. International Conference on Artificial Intelligence & Industrial Engineering, (2015)
22. Prakash, C., Sekar, K.S.V.: 3D finite element analysis of slot milling of unidirectional glass fiber reinforced polymer composites. *J. Braz. Soc. Mech. Sci. Eng.* **40**(6), 279–292 (2018)
23. Abena, A., Soo, S.L., Essa, K.: Modelling the orthogonal cutting of UD-CFRP composites: Development of a novel cohesive zone model. *Compos. Struct.* **168**, 65–83 (2017)
24. Shi, Y., Pinna, C., Soutis, C.: Modelling impact damage in composite laminates: A simulation of intra- and inter-laminar cracking. *Compos. Struct.* **114**(8), 10–19 (2014)
25. Iliescu, D., Gehin, D., Iordanoff, I.: A discrete element method for the simulation of CFRP cutting. *Compos. Sci. Technol.* **70**(1), 73–80 (2010)
26. Hashin, Z., Rotem, A.: A fatigue failure criterion for fiber reinforced materials. *J. Compos. Mater.* **7**(4), 448–464 (1973)
27. Hashin, Z.: Failure criteria for uni-directional fibre composites. *J. Appl. Mech.* **47**(1), 329–334 (1980)
28. Shi, Y., Pinna, C., Soutis, C.: Impact Damage Characteristics of Carbon Fibre Metal Laminates: Experiments and Simulation. *Appl. Compos. Mater.* **27**, 511–531 (2020)
29. Patel, S., Vusa, V.R., Soares, C.G.: Crashworthiness analysis of polymer composites under axial and oblique impact loading. *Int. J. Mech. Sci.* **156**, 221–234 (2019)
30. Puck, A., Schurmann, H.: Failure analysis of FRP laminates by means of physically based phenomenological models. *Compos. Sci. Technol.* **58**, 1045–1067 (1998)
31. Faggiani, A., Falzon, B.G.: Predicting low-velocity impact damage on a stiffened composite panel. *Compos. A.* **41**(6), 737–749 (2010)
32. Knops, M.: Analysis of failure in fiber polymer laminates – the theory of Alfred Puck. Springer, Germany (2008)
33. Shi, Y., Swati, T., Soutis, C.: Modelling damage evolution in composite laminates subjected to low velocity impact. *Compos. Struct.* **94**, 2902–2913 (2012)
34. Wang, F., Wang, X., Zhao, X.: A numerical approach to analyze the burrs generated in the drilling of carbon fiber reinforced polymers (CFRPs). *Int. J. Adv. Manuf. Tech.* **106**(7–8), 3533–3546 (2020)
35. Isbilir, O., Ghassemieh, E.: Three-dimensional numerical modelling of drilling of carbon fiber-reinforced plastic composites. *J. Compos. Mater.* **48**(10), 1209–1219 (2014)
36. Calzada, K.A., Kapoor, S.G., Devor, R.E.: Modeling and interpretation of fiber orientation-based failure mechanisms in machining of carbon fiber-reinforced polymer composites. *J. Manuf. Processes.* **14**(2), 141–149 (2012)
37. Abena, A., Sein, L.S., Khamis, E.: A finite element simulation for orthogonal cutting of UD-CFRP incorporating a novel fibre-matrix interface model. *Procedia. Cirp.* **31**, 539–544 (2015)
38. Nayak, D., Bhatnagar, N., Mahajan, P.: MACHINING STUDIES OF UD-FRP COMPOSITES PART 2: FINITE ELEMENT ANALYSIS. *Mach. Sci. Technol.* **9**(4), 503–528 (2005)